

A topological mechanism for robust and efficient global oscillations in biological networks

Chongbin Zheng^{1,2} and Evelyn Tang^{1,2}

¹*Department of Physics and Astronomy, Rice University, Houston, Texas 77005, USA*

²*Center for Theoretical Biological Physics, Rice University, Houston, Texas 77005, USA*

Stable collective dynamics are often observed in complex biochemical networks, such as in emergent oscillations. How these robust dynamics persist remains unclear, given the many stochastic reactions and shorter time scales demonstrated by underlying components. We propose a topological model that utilizes dissipative motifs to produce emergent oscillations at the network boundary, effectively reducing the system dynamics to a lower-dimensional space. Using this to model KaiC, which regulates the circadian rhythm in cyanobacteria, we compare the coherence of oscillations to that in other KaiC models. Our topological model localizes currents on the system edge which allows for an efficient regime with simultaneously increased precision and decreased cost. Further, we introduce a new predictor of coherence from the analysis of spectral gaps, and show that our model saturates a global thermodynamic bound. Our work presents a new mechanism for emergent oscillations in complex biological networks that utilizes dissipative cycles to achieve robustness and efficient performance.

I. INTRODUCTION

The reduction of the full system response to a much lower dimensional description has been observed in many complex biological systems, where the system dynamics or behavior reduce to a much smaller phase space [1–3]. However, we still lack good models that can mechanistically account for this dimensionality reduction, or that remain stable under noise or structural heterogeneity. This is exemplified in computational models of memory, that describe specific attractor states which represent persistent memories [4, 5]. However, attractors tend to drift or lose accuracy with noise and it remains an area of open research on how to retain encoded information in these models [4]. Another example is that of long oscillations, such as the circadian rhythm, which are crucial for the regulation of many processes such as metabolism and replication [6, 7]. It remains unclear how such oscillations with their ~ 24 h period emerge from a large phase space of faster chemical reactions, even while these internally generated clocks are found in all domains of life. The disruption of these clocks either by mutation or clock–environment mismatch leads to decreased health and reproductive fitness in multiple organisms [7–9]. In mammals, circadian disruption can increase the risk for age-related diseases such as cancer and cardiometabolic dysfunction [10, 11].

As biological networks including those mentioned above typically have a large phase space of possible reactions, this renders unfeasible exhaustive searches using other approaches like experiments or numerical simulation [12], underscoring the need for simple conceptual methods to provide insight [13–15]. The development of rigorous theory would also shed light on simple design principles for targeted dynamics in synthetic biological systems [16, 17] or in the engineering of reconfigurable materials, e.g., through dissipative self-assembly [18, 19]. Yet, biology presents challenges for the development of

suitable theory due to being stochastic, heterogeneous, and strongly non-equilibrium [12, 20–22], and hence, the few successful models that exist in biology are often heavily dependent on specific system parameters.

Towards addressing these questions, we propose a mechanism for the dimensional reduction of phase space to robust attractors and long oscillations. Our model draws on recent developments in topological physics, molecular biology and non-equilibrium stochastic thermodynamics. In particular, we examine the strongly non-equilibrium feature of biological systems, and whether common dissipative motifs can work collectively via novel mechanisms to achieve robustness and unexpected efficiency. For instance, “futile cycles” are common non-equilibrium motifs that are so named due to their consumption of ATP only to repeat the same states in the cycle [23, 24]. Yet, these motifs are pervasive in many different biological systems from metabolism to sensory systems, muscular contraction, and protein synthesis – even while their purpose in all these contexts remains unclear. Here, we show that such non-equilibrium motifs can link in a topological manner to support emergent global dynamics that move in a directed fashion around the network boundary.

Such striking dynamics are a feature of topological invariants, which in the last few decades have proved useful for analyzing emergent function as they characterize a property of the entire system [27–30]. In stochastic systems, these invariant describe whether distinct chemical or mechanical configurations have a global pattern of transition rates between them that supports edge states [31]. Edge states reduce the system response to a lower dimensional space and offer a mechanism for the emergence of global cycles within a large space of reactions. Powerfully, this response is insensitive to various types of disorder or noise and can describe robust biological oscillations. These theories could shed light on the fundamental question of why biological function is so robust, e.g., maintaining stable dynamics over long times even in

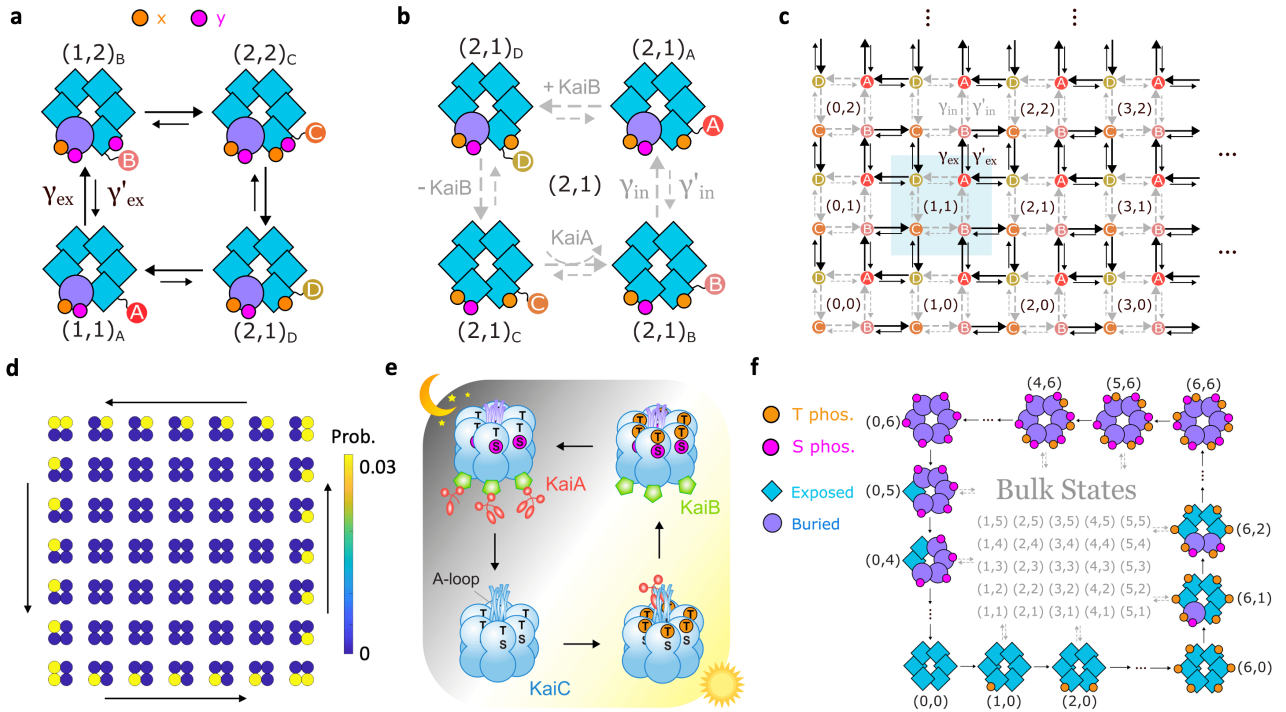


FIG. 1. Topological model for emergent oscillations, illustrated with KaiABC that regulates the circadian rhythm. **a**, Macromolecules exhibit a large space of such reactions, illustrated with a KaiC hexamer. Based on the prevalence of non-equilibrium cycles observed in various biological systems [23, 24], we hypothesize that monomers undergo phosphorylation and dephosphorylation cycles (black arrows γ_{ex} and slower reverse transitions γ'_{ex}), where two types of phosphorylation are shown with the addition of orange and pink circles and the numbers of each are given in brackets. **b**, Within a given phosphorylation level, internal transitions (grey arrows, γ_{in} and γ'_{in}) can take place due to conformational changes (illustrated by circle and square shapes) or ligand binding (e.g., of KaiA or KaiB). **c**, These cycles can be laid out in a lattice, with phosphorylation in orange along the horizontal axis and phosphorylation in purple along the vertical axis, while each set of four internal transitions (e.g., in the blue box) repeats along these axes. **d**, This lattice allows probing of its topological properties. In the ordinary case with similar rates throughout, i.e. $\gamma_{ex} \sim \gamma_{in}$, the system will perform a random walk ergodically through the phase space. In the topological regime when $\gamma_{ex} \gg \gamma_{in}$, once the system hits an edge it will continue around the edge, as can be verified by inspection. We plot the steady-state in the topological regime which lies on the system edge; here $\gamma_{ex} \gg \gamma'_{ex}$ and $\gamma_{in} \gg \gamma'_{in}$. **e**, KaiABC exhibits oscillations via a concerted global cycle of phosphorylation and dephosphorylation. During the day, all six KaiC monomers get phosphorylated at the T-sites, and then at the S-sites. By night, all the T-sites get dephosphorylated, followed by the S-sites. Since individual monomers can independently phosphorylate and shuffle between hexamers [25, 26], why do they perform a concerted phosphorylation cycle that is robust? **f**, We map the reaction space of KaiC onto this lattice, where each hexamer takes phosphorylation levels from (0, 0) to (6, 6). The circle and square represent the buried and exposed conformations of the A-loop (legend), while other internal transitions are modulated by ligand binding. In the topological regime, a global cycle emerges similar to the experimentally observed phosphorylation sequence.

the presence of stochasticity or changing external stimuli. While topological invariants have been heavily studied in quantum electronic systems and been observed in other classical platforms such as mechanical lattices [32, 33], they have not yet been identified in biological systems. Here, we formulate topological methods in the context of stochastic systems and non-equilibrium thermodynamics to quantify the emergence of global cycles that naturally describe biological oscillations. As an example, we illustrate these methods in the context of KaiABC that regulates the circadian rhythm of cyanobacteria [34]. We find that this model exhibits a novel regime with increasing coherence alongside decreasing entropy production, and high coherence compared to other models of KaiABC.

Further, we introduce spectral gaps as a predictor of coherence, and examine the saturation of global spectral bounds.

Interestingly, our approach suggests an alternative mechanism for oscillations from what is typically assumed in the field, such as the Monod-Wyman-Changeux (MWC) paradigm [35]. This paradigm assumes cooperative all-or-none conformational changes for protomers in an oligomer upon ligand binding, which acts as a molecular switch that changes the affinity of all binding sites. The model has been useful in describing systems such as hemoglobin [35], ligand-gated ion channels [36], and bacterial chemotaxis [37]. Still, it remains unclear if the MWC model is the dominant mechanism

for other systems. Indeed, models for KaiABC typically assume highly cooperative conformational changes for KaiC monomers in order to obtain oscillations [38–41]. However, new structural studies suggest that the positive cooperativity between monomer conformational states is fairly weak [42]. Hence, it is timely to examine alternative models that can generate emergent oscillations for macromolecules in the presence of strong internal fluctuations or weak positive cooperativity. Towards this goal, our work proposes a new pathway for the emergence of high coherence despite stochasticity and individual monomer fluctuations, providing a different mechanism to obtain the advantages typically viewed as stemming from strong cooperativity.

II. TOPOLOGICAL MODEL FOR EMERGENT OSCILLATIONS

We consider discrete stochastic processes that operate in a two-dimensional configuration space. The state of the system is described by two integers (x, y) [31]. These two coordinates could represent, for instance, two types of modifications (e.g. phosphorylation) applied to monomers that make up a fixed-size structure such as a protein complex. They could also represent the state of a biopolymer assembled from two types of monomers, X and Y, or from monomers of a single type X that can be modified. The latter scenarios have been discussed in Tang *et al.* [31]; here we illustrate the first case in Fig. 1a, where x and y correspond to two types of phosphorylations acting on monomers of a hexameric molecule, represented by orange and pink circles respectively.

Based on the presence of many non-equilibrium cycles fueled by the consumption of ATP or GTP in a variety of biological systems from metabolism, sensory systems, muscular contraction, and protein synthesis [23, 24], we propose that monomers in our model undergo phosphorylation and dephosphorylation cycles with external transition rates γ_{ex} and slower reverse rates γ'_{ex} . Within each phosphorylation level (x, y) , we specify four internal states labeled by A, B, C, or D, that determine the subsequent reaction, e.g., between phosphorylation or dephosphorylation and whether in the orange or pink space. These states can transition between each other through molecular processes such as conformational changes or ligand binding. These are illustrated in Fig. 1b, where two monomer conformations are distinguished by purple circles and blue squares. These internal transitions are labeled by grey dashed arrows with transition rates γ_{in} and reverse rates γ'_{in} , also forming closed cycles in configuration space.

These reactions are repeated for each monomer and hence can be laid out as a lattice, in which phosphorylation in orange forms the x -axis, and phosphorylation in pink forms the y -axis (see Fig. 1c). The phosphorylation/dephosphorylation cycles in Fig. 1a and the internal cycles in Fig. 1b both repeat along these axes. Such a lattice

will have edges representing the physical constraints of the system, i.e., $0 \leq x \leq N_x$ and $0 \leq y \leq N_y$. In our case, N_x and N_y denote the total number of sites available for phosphorylation in orange and pink respectively, in the protein complex.

Considering the regime where forward rates dominate over the reverse rates, i.e. $\gamma_{ex} \gg \gamma'_{ex}$ and $\gamma_{in} \gg \gamma'_{in}$, there will be two dynamical regimes in this system [31]. In the first case, both types of rates are similar, i.e., $\gamma_{ex} \sim \gamma_{in}$. As each of these rates describe cycles with opposite chirality, the system will simply perform a random walk in configuration space, ergodically exploring the full state space with time. Instead, in the topological regime when $\gamma_{ex} \gg \gamma_{in}$ [31], the system supports an edge state, i.e. once the system reaches the edge it will continue around the edge, which can be verified by inspection in Fig. 1c (also see Supplementary Movie). At long times, the steady-state distribution will hence lie on the system edge; see Fig. 1d. This edge state further inherits the useful property of topological protection from missing components or inaccessible states [31] (see Supplementary Fig. S1).

Thus far, we have been describing a family of networks that can be mapped onto various concrete systems, with their general features and supported dynamics. Specializing to the KaiABC system, KaiC is a hexamer [44] consisting of monomers which each have T and S phosphorylation sites [45] (see Fig. 1e). KaiC exhibits 24-hour cycles via a concerted phosphorylation sequence. During the day, all six KaiC monomers get phosphorylated at the T-sites, and then at the S-sites. By night, all the T-sites get dephosphorylated, again followed by the S-sites [46]. The phosphorylation phase in the day is facilitated by interaction with KaiA [47], while the dephosphorylation phase at night is promoted by binding to KaiB [48]. The robustness of this concerted phosphorylation sequence is surprising, given the large phase space of possible reactions. For instance, it is known that the monomers can assemble into hexamers and disassemble stochastically, and exhibit directed autophosphorylation-dephosphorylation cycles [25]. Monomers also shuffle between different hexamers [26] and display different conformations (exposed or buried A-loops) within the same hexamer [42]. Given this very large phase space of possible reactions available to individual monomers, why would all the monomers phosphorylate together in a concerted global cycle? Further, since phosphorylation in both T and S are promoted during the day, why does phosphorylation proceed in the specific order where all six T sites get phosphorylated before S phosphorylation begins (Fig. 1e)? To answer this question, models [38–41] have typically relied on the concerted or Monod-Wyman-Changeux paradigm [35] of allosteric regulation, which restricts the configuration space such that either all or none of the monomers in a complex undergo a conformational change. However, recent cryo-EM data shows that monomers demonstrate independent conformational changes within the same hexamer [42], challenging this

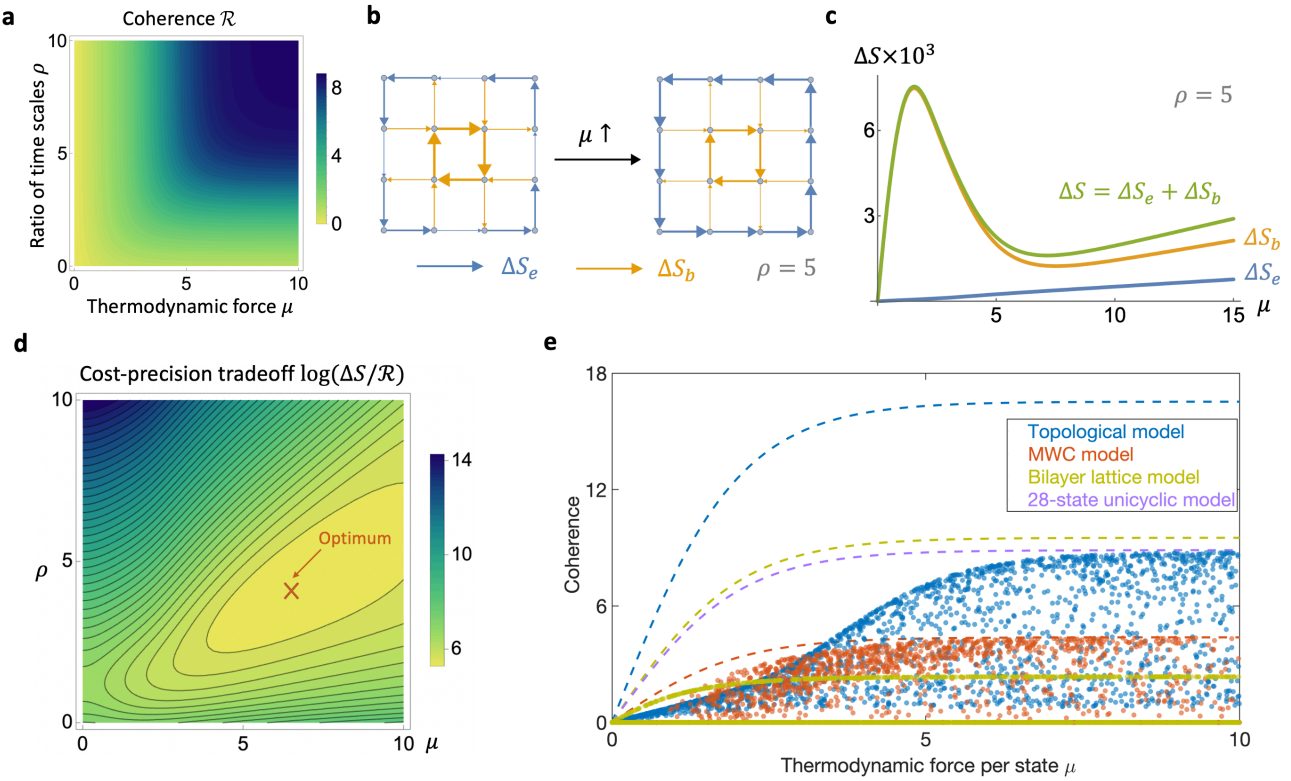


FIG. 2. Coherence and an efficient regime with simultaneously increased precision and decreased cost. **a**, Phase diagram of coherence \mathcal{R} for the topological model, which increases with respect to thermodynamic force μ and ratio of timescales ρ as expected. **b**, Entropy production ΔS moves from the bulk to the boundary of the system with increasing μ , illustrated on a smaller lattice. The system is in the topological regime; $\rho = 5$. Blue arrows represent entropy production on the edge ΔS_e and orange arrows represent entropy production in the bulk ΔS_b ; arrow thickness corresponds to the magnitude of the entropy production. **c**, Entropy production per period ΔS for the topological model is decomposed into a bulk and an edge contribution. Due to the localization effects in Fig. 2b, the entropy production on the edge ΔS_e (blue) increases while entropy production in the bulk ΔS_b (orange) decreases with μ . Typically, the bulk contribution dominates the edge contribution, hence their sum ΔS (green) also decreases with increasing μ . **d**, Phase diagram of the cost-precision tradeoff $\Delta S/\mathcal{R}$: there is a global optimum at $\mu = 6.5, \rho = 4.1$ due to the non-monotonic behavior of ΔS that suggests an unusual efficient regime. **e**, Comparison of coherence for different KaiC models with randomly sampled parameters (individual points): there is a strongly-driven regime where the topological model has the highest coherence. The dashed lines represent the upper bounds on coherence for the corresponding models [43]. The purple dashed line is the upper bound for the 28-state unicyclic model, which is approached by the edge state in the strongly topological regime. ΔS values in all panels are given in units of $\gamma_{tot}k_B$.

strong restriction. Further, these models often put in by hand the specific ordering of T-site phosphorylation occurring before S-site phosphorylation.

To propose an alternative model, we map the reaction space of KaiC onto our lattice model. Based on experimental evidence for KaiC monomer autophosphorylation [25, 26], we hypothesize that monomer undergo directed cycles of phosphorylation and dephosphorylation where the x and y coordinates in Fig. 1a represent T phosphorylation (orange) and S phosphorylation (pink) respectively (see Fig. 1f legend). KaiC monomers also have internal conformational changes in the A-loop, interact with KaiA, and bind to KaiB with transition rates $\gamma_{in} \gg \gamma'_{in}$, which also form directed cycles (see Fig. 1b). In turn, the blue squares and purple circles in Fig. 1b corresponds to the exposed and buried conformations of the A-loop (see Fig. 1f). KaiA, in particular, promotes

phosphorylation through rapid association and dissociation with KaiC molecules (Fig. 1b), activating a larger stoichiometric amount of KaiC than expected from simple one-to-one interactions [26].

Our hypothesis that KaiA and KaiB preferentially interact with different phosphorylation configurations in our model is consistent with experimental evidence that activation by KaiA is incompatible with the configuration of KaiC that triggers KaiB binding [26]. In particular, we propose that KaiA preferentially interacts with KaiC during T-site phosphorylation rather than S-site phosphorylation, and the converse for KaiB, which agrees with observed data [49]. Indeed, experiments indicate that KaiB binding (and possibly its unbinding), which have γ_{in} in our model, are slow processes [26, 50–52] compared to phosphorylation reactions (which have γ_{ex} in our model) [39] — consistent with our assumption

that there is a separation of timescales. Lastly, we assume that the A-loop for a monomer changes from the exposed to the buried state following S-site phosphorylation of the same monomer, consistent with experimental results that S-site phosphorylation stabilizes the buried state [53]. This gives rise to our model assigning the internal states B and C of a given (x, y) state (for $y > 0$) as having $y - 1$ circles (denoting $y - 1$ buried A-loops) and $7 - y$ diamonds (denoting $7 - y$ exposed A-loops), while the internal states A and D of a state (x, y) have y circles and $6 - y$ diamonds.

These reactions now form the same lattice as shown in Fig. 1c, where now the indices range from $(0, 0)$ to $(6, 6)$ for a hexameric molecule. As discussed above, in the topological regime where $\gamma_{ex} \gg \gamma_{in}$ the system supports a propagating edge current (Fig. 1d). As we can see in Fig. 1f, the edge current is equivalent to a global cycle of concerted phosphorylation of the T-sites, followed by the S-sites, then dephosphorylation of the T-sites and, lastly, of the S-sites (also see Supplementary Movie). This provides a mechanism that allows for individual monomers to undergo conformational and other changes, while still producing a global cycle and the experimentally observed phosphorylation sequence that emerges with less fine-tuning. Note that Fig. 1f is a coarse-grained picture in which only one of the four internal states is shown for each (x, y) phosphorylation level, specifically the last state along the edge (e.g. B states for the bottom edge or C states for the left edge).

III. MODEL THERMODYNAMICS: PRECISION VS COST

While this topological model provides an unique alternative mechanism to experimentally observed oscillatory dynamics, how precise or efficient are the oscillations produced? In this section, we quantify the thermodynamics and entropy production of this model, and compare its performance to that of other KaiC models [43, 54, 55]. Further, we identify a new predictor for oscillator coherence and analyze the saturation of thermodynamic bounds for different models. We begin by analyzing the master equation that describes stochastic systems,

$$\frac{d\mathbf{p}}{dt} = \mathcal{W}\mathbf{p}, \quad (1)$$

where $\mathbf{p}(t)$ is a vector that describes the probability distribution of system states. \mathcal{W} is the transition matrix, whose elements \mathcal{W}_{ij} specify the transition rates from state j to i . The dynamics of oscillations is typically dominated by the first non-zero eigenvalue of \mathcal{W} , where λ_R and λ_I are its real and imaginary parts. In general, $\mathbf{p}(t)$ relaxes to the steady-state distribution through damped oscillations, with a decay time $|\lambda_R^{-1}|$ and oscillation period $\mathcal{T} = 2\pi/|\lambda_I|$ [43] (also see Supplementary Fig. S2).

Following [43], coherence is defined as the ratio

$$\mathcal{R} \equiv \left| \frac{\lambda_I}{\lambda_R} \right|, \quad (2)$$

which quantifies the robustness of sustained oscillations before stochastic noise destroys the coherence (more details in Supplementary Information). We would like to see how our model performs using this metric and what factors contribute to increased coherence.

In typical oscillator models, coherence can be increased by dissipating more free energy. For example, in the MWC-type model of KaiC studied in [43], increasing the entropy production per period ΔS is necessary to increase coherence (see Supplementary Fig. S5). ΔS is defined as

$$\Delta S = \frac{\mathcal{T}}{2} \sum_{i,j} (p_j^s \mathcal{W}_{ij} - p_i^s \mathcal{W}_{ji}) \ln \left(\frac{p_j^s \mathcal{W}_{ij}}{p_i^s \mathcal{W}_{ji}} \right) \quad (3)$$

for the steady-state probability distribution \mathbf{p}^s and oscillation period \mathcal{T} [56, 57]. It quantifies the free energy cost to maintain the system in a non-equilibrium steady-state, and increases with thermodynamic driving for the MWC model.

Before analyzing our topological model, we simplify our notation. Our four rates for external and internal transitions γ_{ex} and γ_{in} and their reverse γ'_{ex} and γ'_{in} can be simplified with two parameters. First, μ is the thermodynamic force defined by $e^{\mu/k_B T} \equiv \gamma_{ex}/\gamma'_{ex} = \gamma_{in}/\gamma'_{in}$, that characterizes how much the system is being driven. Detailed balance occurs at $\mu = 0$ while out-of-equilibrium is when $\mu > 0$; we analyze μ in units of $k_B T$. Second, ρ varies the ratio of external to internal transitions, where $e^\rho \equiv \gamma_{ex}/\gamma_{in} = \gamma'_{ex}/\gamma'_{in}$ and quantifies the separation of timescales between the external and internal transitions. $\rho > 0$ is the topological regime that supports edge states while $\rho < 0$ is the trivial regime with random diffusion. The sum of all transition rates in the system is $\gamma_{tot} \equiv \gamma_{ex} + \gamma'_{ex} + \gamma_{in} + \gamma'_{in}$.

We now study the coherence of our model with respect to these two parameters (Fig. 2a; also see Supplementary Fig. S3). Both increasing the thermodynamic force μ and going deeper into the topological regime by increasing ρ , each increase oscillation coherence as expected. However, the entropy production per period ΔS , does not change monotonically with μ . As illustrated in Fig. 2b in a smaller lattice, the system response becomes localized to the edge as μ increases. This causes the entropy production on the edge to increase, while the entropy production in the bulk decreases (blue and orange curves respectively in Fig. 2c). Since the bulk contribution typically dominates the edge contribution, i.e. $\mathcal{O}(N^2) \gg \mathcal{O}(N)$ where N is the typical system size, the sum of their contributions also decreases (green curve in Fig. 2c). Meanwhile, since coherence increases monotonically with μ , this leads to an efficient regime with simultaneously increasing coherence and decreasing cost – see Fig. 2d for the region in parameter space that optimizes the cost-precision trade-off $\Delta S/\mathcal{R}$.

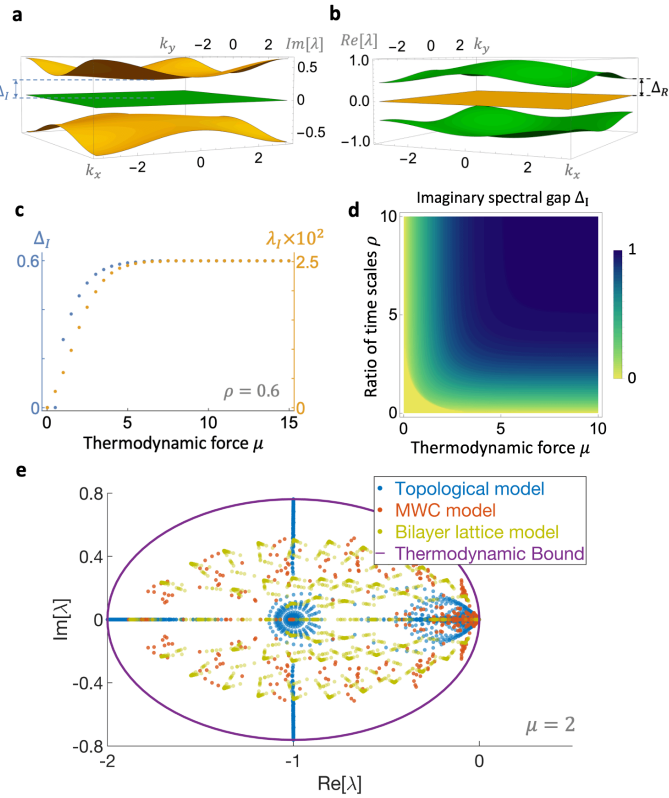


FIG. 3. New predictor of coherence and saturation of a global thermodynamic bound. **a,b**, Spectrum for the topological model in reciprocal space in imaginary space (**a**) and real space (**b**) for $\mu = 1.5$ and $\rho = 1$. The spectral gaps Δ_I and Δ_R are defined as the difference between the minimum of the topmost band and the maximum of the second band. **c**, The imaginary spectral gap Δ_I closely tracks the imaginary part of the first non-zero eigenvalue λ_I , as a function of μ . **d**, Phase diagram for the imaginary spectral gap Δ_I in μ and ρ . Δ_I and coherence (Fig. 2a) track each other monotonically, and both saturate to a maximum value after a rapid increase. **e**, The global spectral bound for a fixed μ is shown by a purple ellipse in the complex plane [58], while points represent the transition matrix \mathcal{W} spectra for different oscillator models. The topological model approaches this bound in the limit $\rho \rightarrow \infty$, which is saturated by the most coherent cycle (the unicycle) [58]. Here $\mu = 2$ and other parameters are randomly sampled. In all panels, eigenvalues are given in units of γ_{tot} .

We can further compare coherence between different families of KaiC models. We include a simple MWC-type model [43] and a bilayer model that has a lattice structure more similar to ours, adapted from Li et al. [55] (details of each in Supplementary Information). Note that the bilayer lattice represents the T and S phosphorylation levels along its x and y coordinates similar to our topological model, with the possibility to switch between two layers that denote unbound KaiC and KaiB-bound KaiC, respectively (See Supplementary Fig. S4b). KaiC is more likely to bind to KaiB on the upper right half of each lattice and more likely to unbind on the lower

left half. In order to aid comparison, we simplified this lattice model using our (μ, ρ) parameters (details in Supplementary Information).

By sampling random parameters in the three models, we find a regime of high thermodynamic driving where the topological model has the highest coherence (Fig. 2e). In the same plot, we also indicate the conjectured thermodynamic bounds for coherence [43] for each model (dashed lines), which depend on the system size and thermodynamic force μ (see Methods). We also plot the bound for a 28-state unicyclic model (purple dashed line in Fig. 2e), which our model approaches in the limit of high μ and high ρ . This is because there are 28 slow internal transitions on the edge that form the effective bottleneck and dominate over the other fast external transitions. This shows that our topological model approaches the bound set by the most coherent cycle, which is the unicycle with uniform rates [43], deep in the topological regime with high external driving.

Given the high coherence of our model, we would like to identify the factors that determine high coherence. Here, we introduce a new predictor of coherence, which is the spectral gap (or band gap) of the system, inspired from band theory [59]. As the spectral gap measures the separation between modes with different timescales [56], a larger gap predicts greater separation between modes and hence the stability of longer-lived modes as they mix less with transient ones. See Fig. 3a and 3b for the spectral gap in both imaginary and real space, Δ_I and Δ_R respectively, in the reciprocal space version of our topological model (see Supplementary Information for more details). The spectral gap is defined as the difference between the minimum of the topmost band and the maximum of the band below it. Comparing Δ_I with the imaginary part λ_I of the first non-zero eigenvalue in Fig. 3c, we see that they track each other well as μ is increased. Since coherence \mathcal{R} is the ratio of λ_I to its corresponding real part λ_R of the same eigenvalue (Eq. 2) and λ_R remains roughly constant with increasing μ (see Supplementary Fig. S7), Δ_I tracks \mathcal{R} (Fig. 2a) monotonically in μ as well. Along the other axis, increasing ρ decreases the spectral dispersion, i.e. it compresses the top band in Fig. 3a. The topmost point of the top band also increases with ρ while the lower bands (green bands in Fig. 3a) remain flat, leading to a widened spectral gap Δ_I for increasing ρ . Moreover, $|\lambda_R|$ decreases more quickly than $|\lambda_I|$ with increasing ρ , so that their ratio \mathcal{R} increases (see Supplementary Fig. S7). Therefore, Δ_I tracks coherence in ρ as well. Hence, both the imaginary spectral gap and coherence track each other monotonically, as can be seen in their phase diagrams Figs. 3d and 2a respectively, where both saturate to a maximum following a rapid increase.

Lastly, we examine how the different models perform compared to a conjectured global thermodynamic bound on the full spectrum of \mathcal{W} [58]. For a given thermodynamic force, the spectrum is found to lie within an ellipse in the complex plane (purple line in Fig. 3e). The most coherent cycle, a unicyclic network with uniform rates

[43], saturates this bound [58]. While the other two families of KaiC models do not saturate the bound for any sampled parameters, our model approaches this bound as $\rho \rightarrow \infty$. This is consistent with our model approaching a uniform unicyclic network when ρ is large, and also with our previous analysis of the spectral gap contributing to high coherence. Similar to the results in reciprocal space model discussed above, the transition matrix \mathcal{W} also shows a larger imaginary spectral gap as ρ increases, which moves the topmost eigenvalue upward in the complex plane and saturates the global spectral bound while increasing coherence (see Supplemental Information and Fig. S6 for details).

IV. DISCUSSION

We have proposed a topological model that generates coherent oscillations, which supports an unusual regime with increased coherence and simultaneously decreased energetic cost. We find that the imaginary spectral gap can be used to predict the oscillation coherence. Applied to the KaiABC system, our model has high coherence compared to other KaiABC models and more closely saturates a global spectral bound, similar to the most coherent unicyclic models. Further, the kinetic ordering of the KaiABC phosphorylation cycle arises naturally as an edge current in our model. In contrast to typical MWC-type models, it does not require restriction of the configuration space to all-or-none conformational change or fine-tuning of the reaction rates to generate the experimentally observed phosphorylation sequence.

We further predict testable signatures of topological edge states in biological oscillators and the KaiABC system. Examining our steady-state distribution (Fig. 1d), we expect to find mixtures of molecules with specific fractions of differentially phosphorylated subunits, where such mixtures have been experimentally observed [49]. Here, KaiB-bound KaiC should be less abundant than unbound KaiC, because the slow γ_{in} transitions cause a buildup of the latter before they bind to KaiB. Moreover, new innovations in calorimetric techniques for the heat fluxes involved in the cell cycle could estimate the amount of energy dissipation in the production of oscillations,

which intriguingly highlight the strong contribution of non-equilibrium cycles [60], similar to our hypothesis. As for transient dynamics, monomer phosphorylation cycles in the reverse direction from the global cycle may also be observed, as the external cycles in the system bulk have the opposite chirality from our global cycle on the system edge (see Fig. 1c).

Our model gives rise to the observed sequence of phosphorylation reactions in KaiABC without having to tune as many free parameters as in typical models [38, 39]. This is due to the repetition of simple motifs in our network, such that these motifs are governed by only a handful of free parameters. Further, we note that population effects in KaiABC are known to be important, e.g., by promoting the synchronization of many molecules in the KaiABC system [38, 50, 61]. Still, the oscillation and coherence of individual molecules are generally presumed to be building blocks for sustained oscillations at the population level, even while the extent of the single-molecule contribution remains unclear. Hence, our work focuses on the oscillations and coherence of single molecules as a first step towards the understanding of population-level coherence more generally, with the exploration of multiples molecules and their synchronization to be left for future work.

By rigorously embedding topological methods within non-equilibrium statistical physics, our work generalizes their usage for various biological and chemical systems. Our results suggest a new mechanism that utilizes dissipative cycles to produce emergent oscillations or attractor states in biological systems. This mechanism can be tested by introducing perturbation or mutant proteins [62], in order to jointly analyze how these changes modify the robustness and coherence of the global cycle. More broadly, our models provides a blueprint for the design for synthetic oscillators, which is becoming increasingly feasible due to new experimental developments [63, 64]. While designing synthetic oscillators that are robust across different parameters or changes in the environment remains a challenge [65, 66], this project provides new models for robust oscillators and continuous attractor dynamics in various biochemical scenarios and changing conditions.

[1] M. Rigotti, O. Barak, M. R. Warden, X.-J. Wang, N. D. Daw, E. K. Miller, and S. Fusi, The importance of mixed selectivity in complex cognitive tasks, *Nature* **497**, 585 (2013).

[2] E. Tang, M. G. Mattar, C. Giusti, D. M. Lydon-Staley, S. L. Thompson-Schill, and D. S. Bassett, Effective learning is accompanied by high-dimensional and efficient representations of neural activity, *Nature neuroscience* **22**, 1000 (2019).

[3] G. J. Stephens, B. Johnson-Kerner, W. Bialek, and W. S. Ryu, Dimensionality and dynamics in the behavior of *C. elegans*, *PLoS computational biology* **4**, e1000028 (2008).

[4] R. Chaudhuri and I. Fiete, Computational principles of memory, *Nature neuroscience* **19**, 394 (2016).

[5] J. J. Hopfield, Neural networks and physical systems with emergent collective computational abilities., *Proceedings of the national academy of sciences* **79**, 2554 (1982).

[6] Y. Liao and M. J. Rust, The circadian clock ensures successful dna replication in cyanobacteria, *Proceedings of the National Academy of Sciences* **118**, e2022516118 (2021).

[7] A. M. Puszynska and E. K. O’Shea, Switching of

metabolic programs in response to light availability is an essential function of the cyanobacterial circadian output pathway, *elife* **6**, e23210 (2017).

[8] R. M. Green, S. Tingay, Z.-Y. Wang, and E. M. Tobin, Circadian rhythms confer a higher level of fitness to *Arabidopsis* plants, *Plant physiology* **129**, 576 (2002).

[9] M. Horn, O. Mitesser, T. Hovestadt, T. Yoshii, D. Rieger, and C. Helfrich-Förster, The circadian clock improves fitness in the fruit fly, *Drosophila melanogaster*, *Frontiers in Physiology* **10**, 1374 (2019).

[10] F. A. Scheer, M. F. Hilton, C. S. Mantzoros, and S. A. Shea, Adverse metabolic and cardiovascular consequences of circadian misalignment, *Proceedings of the National Academy of Sciences* **106**, 4453 (2009).

[11] S. Masri and P. Sassone-Corsi, The emerging link between cancer, metabolism, and circadian rhythms, *Nature medicine* **24**, 1795 (2018).

[12] A. L. Dewyer, A. J. Argüelles, and P. M. Zimmerman, Methods for exploring reaction space in molecular systems, *Wiley Interdisciplinary Reviews: Computational Molecular Science* **8**, e1354 (2018).

[13] P. Davies, Does new physics lurk inside living matter?, *Physics today* **73**, 34 (2020).

[14] A. T. Winfree, *The geometry of biological time*, Vol. 2 (Springer, 1980).

[15] P. Gao and S. Ganguli, On simplicity and complexity in the brave new world of large-scale neuroscience, *Current opinion in neurobiology* **32**, 148 (2015).

[16] J. Doudna, R. Bar-Ziv, J. Elf, V. Noireaux, J. Berro, L. Saiz, D. Vavylonis, J.-L. Faulon, and P. Fordyce, How will kinetics and thermodynamics inform our future efforts to understand and build biological systems?, *Cell Systems* **4**, 144 (2017).

[17] P. Schwille, J. Spatz, K. Landfester, E. Bodenschatz, S. Herminghaus, V. Sourjik, T. J. Erb, P. Bastiaens, R. Lipowsky, A. Hyman, *et al.*, MaxSynBio: avenues towards creating cells from the bottom up, *Angewandte Chemie International Edition* **57**, 13382 (2018).

[18] J. Deng and A. Walther, ATP-Responsive and ATP-Fueled Self-Assembling Systems and Materials, *Advanced Materials* **32**, 2002629 (2020).

[19] B. Rieß, R. K. Grötsch, and J. Boekhoven, The design of dissipative molecular assemblies driven by chemical reaction cycles, *Chem* **6**, 552 (2020).

[20] J. Ross and A. P. Arkin, Complex systems: from chemistry to systems biology, *Proceedings of the National Academy of Sciences* **106**, 6433 (2009).

[21] G. Ashkenasy, T. M. Hermans, S. Otto, and A. F. Taylor, Systems chemistry, *Chemical Society Reviews* **46**, 2543 (2017).

[22] H. Qian and H. Ge, *Stochastic Chemical Reaction Systems in Biology* (Springer, 2021).

[23] J. J. Hopfield, Kinetic proofreading: a new mechanism for reducing errors in biosynthetic processes requiring high specificity, *Proceedings of the National Academy of Sciences* **71**, 4135 (1974).

[24] M. Samoilov, S. Plyasunov, and A. P. Arkin, Stochastic amplification and signaling in enzymatic futile cycles through noise-induced bistability with oscillations, *Proceedings of the National Academy of Sciences* **102**, 2310 (2005).

[25] C. Brettschneider, R. J. Rose, S. Hertel, I. M. Axmann, A. J. Heck, and M. Kollmann, A sequestration feedback determines dynamics and temperature entrainment of the KaiABC circadian clock, *Molecular Systems Biology* **6**, 389 (2010).

[26] H. Kageyama, T. Nishiwaki, M. Nakajima, H. Iwasaki, T. Oyama, and T. Kondo, Cyanobacterial circadian pacemaker: Kai protein complex dynamics in the KaiC phosphorylation cycle in vitro, *Molecular cell* **23**, 161 (2006).

[27] J. E. Moore, The birth of topological insulators, *Nature* **464**, 194 (2010).

[28] C.-K. Chiu, J. C. Teo, A. P. Schnyder, and S. Ryu, Classification of topological quantum matter with symmetries, *Reviews of Modern Physics* **88**, 035005 (2016).

[29] H. L. Stormer, D. C. Tsui, and A. C. Gossard, The fractional quantum hall effect, *Reviews of Modern Physics* **71**, S298 (1999).

[30] E. Tang and X.-G. Wen, Interacting one-dimensional fermionic symmetry-protected topological phases, *Physical Review Letters* **109**, 096403 (2012).

[31] E. Tang, J. Agudo-Canalejo, and R. Golestanian, Topology protects chiral edge currents in stochastic systems, *Physical Review X* **11**, 031015 (2021).

[32] C. Kane and T. Lubensky, Topological boundary modes in isostatic lattices, *Nature Physics* **10**, 39 (2014).

[33] R. Süsstrunk and S. D. Huber, Observation of phononic helical edge states in a mechanical topological insulator, *Science* **349**, 47 (2015).

[34] M. Ishiura, S. Kutsuna, S. Aoki, H. Iwasaki, C. R. Andersson, A. Tanabe, S. S. Golden, C. H. Johnson, and T. Kondo, Expression of a gene cluster kaiABC as a circadian feedback process in cyanobacteria, *Science* **281**, 1519 (1998).

[35] J. Monod, J. Wyman, and J.-P. Changeux, On the nature of allosteric transitions: a plausible model, *Journal of molecular biology* **12**, 88 (1965).

[36] N. Calimet, M. Simoes, J.-P. Changeux, M. Karplus, A. Taly, and M. Cecchini, A gating mechanism of pentameric ligand-gated ion channels, *Proceedings of the National Academy of Sciences* **110**, E3987 (2013).

[37] B. A. Mello and Y. Tu, An allosteric model for heterogeneous receptor complexes: understanding bacterial chemotaxis responses to multiple stimuli, *Proceedings of the National Academy of Sciences* **102**, 17354 (2005).

[38] J. S. van Zon, D. K. Lubensky, P. R. Altena, and P. R. ten Wolde, An allosteric model of circadian KaiC phosphorylation, *Proceedings of the National Academy of Sciences* **104**, 7420 (2007).

[39] J. Paijmans, D. K. Lubensky, and P. R. Ten Wolde, A thermodynamically consistent model of the post-translational Kai circadian clock, *PLoS computational biology* **13**, e1005415 (2017).

[40] Y.-G. Chang, R. Tseng, N.-W. Kuo, and A. LiWang, Rhythmic ring-ring stacking drives the circadian oscillator clockwise, *Proceedings of the National Academy of Sciences* **109**, 16847 (2012).

[41] D. Zhang, Y. Cao, Q. Ouyang, and Y. Tu, The energy cost and optimal design for synchronization of coupled molecular oscillators, *Nature physics* **16**, 95 (2020).

[42] X. Han, D. Zhang, L. Hong, D. Yu, Z. Wu, T. Yang, M. Rust, Y. Tu, and Q. Ouyang, A cooperative switch within the KaiC hexamer revealed by cryo-EM, *bioRxiv* (2022).

[43] A. C. Barato and U. Seifert, Coherence of biochemical oscillations is bounded by driving force and network topology, *Physical Review E* **95**, 062409 (2017).

[44] R. Pattanayek, J. Wang, T. Mori, Y. Xu, C. H. Johnson,

and M. Egli, Visualizing a circadian clock protein: crystal structure of KaiC and functional insights, *Molecular cell* **15**, 375 (2004).

[45] T. Nishiwaki, Y. Satomi, M. Nakajima, C. Lee, R. Kiyohara, H. Kageyama, Y. Kitayama, M. Temamoto, A. Yamaguchi, A. Hijikata, *et al.*, Role of KaiC phosphorylation in the circadian clock system of *Synechococcus elongatus* PCC 7942, *Proceedings of the National Academy of Sciences* **101**, 13927 (2004).

[46] S. E. Cohen and S. S. Golden, Circadian rhythms in cyanobacteria, *Microbiology and Molecular Biology Reviews* **79**, 373 (2015).

[47] Y. Xu, T. Mori, and C. H. Johnson, Cyanobacterial circadian clockwork: roles of KaiA, KaiB and the kaiBC promoter in regulating KaiC, *The EMBO Journal* **22**, 2117 (2003).

[48] Y. Kitayama, H. Iwasaki, T. Nishiwaki, and T. Kondo, KaiB functions as an attenuator of KaiC phosphorylation in the cyanobacterial circadian clock system, *The EMBO journal* **22**, 2127 (2003).

[49] J. Lin, J. Chew, U. Chockanathan, and M. J. Rust, Mixtures of opposing phosphorylations within hexamers precisely time feedback in the cyanobacterial circadian clock, *Proceedings of the National Academy of Sciences* **111**, E3937 (2014).

[50] M. J. Rust, J. S. Markson, W. S. Lane, D. S. Fisher, and E. K. O'Shea, Ordered phosphorylation governs oscillation of a three-protein circadian clock, *Science* **318**, 809 (2007).

[51] J. Abe, T. B. Hiyama, A. Mukaiyama, S. Son, T. Mori, S. Saito, M. Osako, J. Wolanin, E. Yamashita, T. Kondo, *et al.*, Atomic-scale origins of slowness in the cyanobacterial circadian clock, *Science* **349**, 312 (2015).

[52] D. Simon, A. Mukaiyama, Y. Furuike, and S. Akiyama, Slow and temperature-compensated autonomous disassembly of kaib-kaic complex, *Biophysics and Physicobiology* **19**, e190008 (2022).

[53] R. Tseng, Y.-G. Chang, I. Bravo, R. Latham, A. Chaudhary, N.-W. Kuo, and A. LiWang, Cooperative KaiA-KaiB-KaiC interactions affect KaiB/SasA competition in the circadian clock of cyanobacteria, *Journal of molecular biology* **426**, 389 (2014).

[54] R. Marsland III, W. Cui, and J. M. Horowitz, The thermodynamic uncertainty relation in biochemical oscillations, *Journal of the Royal Society Interface* **16**, 20190098 (2019).

[55] C. Li, X. Chen, P. Wang, and W. Wang, Circadian KaiC phosphorylation: a multi-layer network, *PLoS computational biology* **5**, e1000568 (2009).

[56] J. Schnakenberg, Network theory of microscopic and macroscopic behavior of master equation systems, *Reviews of Modern Physics* **48**, 571 (1976).

[57] H. Ge and H. Qian, Physical origins of entropy production, free energy dissipation, and their mathematical representations, *Physical Review E* **81**, 051133 (2010).

[58] M. Uhl and U. Seifert, Affinity-dependent bound on the spectrum of stochastic matrices, *Journal of Physics A: Mathematical and Theoretical* **52**, 405002 (2019).

[59] C. Kittel, *Solid state physics*, Vol. 3 (Shell Development Company, 1955).

[60] X. Yang, M. Heinemann, J. Howard, G. Huber, S. Iyer-Biswas, G. Le Treut, M. Lynch, K. L. Montooth, D. J. Needleman, S. Pigolotti, *et al.*, Physical bioenergetics: Energy fluxes, budgets, and constraints in cells, *Proceedings of the National Academy of Sciences* **118**, e2026786118 (2021).

[61] M. Nakajima, K. Imai, H. Ito, T. Nishiwaki, Y. Murayama, H. Iwasaki, T. Oyama, and T. Kondo, Reconstitution of circadian oscillation of cyanobacterial KaiC phosphorylation in vitro, *science* **308**, 414 (2005).

[62] A. G. Chavan, J. A. Swan, J. Heisler, C. Sancar, D. C. Ernst, M. Fang, J. G. Palacios, R. K. Spangler, C. R. Bagshaw, S. Tripathi, *et al.*, Reconstitution of an intact clock reveals mechanisms of circadian timekeeping, *Science* **374**, eabd4453 (2021).

[63] V. Klingel, D. Graf, S. Weirich, A. Jeltsch, and N. E. Radde, Model-based design of a synthetic oscillator based on an epigenetic methylation memory system, *ACS Synthetic Biology* **11**, 2445 (2022).

[64] A. H. Chen, D. Lubkowicz, V. Yeong, R. L. Chang, and P. A. Silver, Transplantability of a circadian clock to a noncircadian organism, *Science advances* **1**, e1500358 (2015).

[65] M. L. Woods, M. Leon, R. Perez-Carrasco, and C. P. Barnes, A statistical approach reveals designs for the most robust stochastic gene oscillators, *ACS synthetic biology* **5**, 459 (2016).

[66] Ž. Pušnik, M. Mraz, N. Zimic, and M. Moškon, Computational analysis of viable parameter regions in models of synthetic biological systems, *Journal of biological engineering* **13**, 1 (2019).

[67] D. T. Gillespie, Exact stochastic simulation of coupled chemical reactions, *The journal of physical chemistry* **81**, 2340 (1977).

METHODS

Simulation of the system steady-state. The steady-state probability distribution in Fig. 1d is obtained by simulating the system dynamics with the Gillespie algorithm [67]. The simulation is run for 10^8 steps with a random initial condition, and the probability for each state is given by the fraction of time the system spends in that state. By calculating the steady-state probability flux $J_{ij} = p_j^s \mathcal{W}_{ij} - p_i^s \mathcal{W}_{ji}$ from state j to i , we obtain the global counterclockwise current along the edge of the lattice, illustrated with black arrows in Fig. 1d.

Thermodynamic bound for coherence. Ref. [43] conjectures an upper bound for coherence for any stochastic system. Suppose that a cycle κ has N_κ states labeled by $\kappa_1, \kappa_2, \dots, \kappa_{N_\kappa}$ such that κ_1 is connected to κ_{N_κ} and κ_2 , κ_2 is connected to κ_1 and κ_3 , etc. Define the affinity of κ as $\mathcal{A}_\kappa \equiv \ln \prod_{i=1}^{N_\kappa} \frac{\mathcal{W}_{\kappa_{i+1}\kappa_i}}{\mathcal{W}_{\kappa_i\kappa_{i+1}}}$, where $\kappa_{N_\kappa+1}$ is the same as κ_1 . For an arbitrary stochastic model, we look at all possible cycles in the underlying network. The upper bound for coherence in Fig. 2e is given by

$$\mathcal{R} \leq \max_\kappa \{ \cot(\pi/N_\kappa) \tanh[\mathcal{A}_\kappa/(2N_\kappa)] \}.$$

For the topological model, the thermodynamic force per state $\mathcal{A}_\kappa/N_\kappa$ is always μ , and the cycle that maximizes the right hand side of the bound is the global cycle going around the boundary with $N_\kappa = 52$.

Global spectral bound for a driven stochastic system. The global bound in Fig. 3e is conjectured by [58] for the spectrum of any transition matrix for a master equation. To obtain the bound, we look for a cycle that maximizes the affinity per state $\mathcal{A}_\kappa/N_\kappa$. Denote this

maximum by \mathcal{A}_C/N_C . We also define $w_0 = \max_i [|\mathcal{W}_{ii}|]$. The spectrum is hypothesized to lie entirely in the ellipse given by

$$g(x) = w_0 \{ -1 + \cos(2\pi x) + i \tanh[\mathcal{A}_C/(2N_C)] \sin(2\pi x) \}.$$

For the topological model, we have $\mathcal{A}_C/N_C = \mu$. The bound for $\mu = 2$ is plotted in purple in Fig. 3e. Each model has a different w_0 for their corresponding transition matrix. To plot all spectra under a common bound, we rescale each transition matrix by a constant factor such that $w_0 = 1$ for all transition matrices considered.

Sampling random parameters In Fig. 2e, for the topological model and the bilayer lattice model, we randomly select the parameters $\mu \in [0, 10]$ and $\rho \in [0, 7]$ from uniform distributions on each interval. For the MWC model in [43] (see Supplementary Information for parameter definitions), we select from the uniform distributions $\gamma \in [3, 7]$, $E \in [5, 15]$ and $\eta \in [0, \frac{70}{3}]$. The parametrization of the MWC model is such that the maximum affinity per state is $\mathcal{A}/N = \frac{3}{7}\eta$. Because we keep \mathcal{A}/N (which we also call thermodynamic force per state and simply denote as μ) the same in Fig. 2e, $\eta \in [0, \frac{70}{3}]$ exactly corresponds to $\mu \in [0, 10]$. For Fig. 3e, we fix the thermodynamic force per state $\mu = 2$ (which is $\eta = \frac{14}{3}$ for the MWC model) and sample the remaining parameters ρ , γ , and E in the same way as above.

ACKNOWLEDGEMENT

We are grateful to Jordan Horowitz, David Lubensky, Jaime Agudo-Canalejo and Yuhai Tu for helpful discussions. In addition, we thank Pankaj Mehta, Peter Wolynes, Ulrich Schwarz and Oleg Igoshin for their thoughtful comments.

Supplementary Information for “A topological mechanism for robust and efficient global oscillations in biological networks”

Chongbin Zheng^{1,2} and Evelyn Tang^{1,2}

¹*Department of Physics and Astronomy, Rice University, Houston, Texas 77005, USA*

²*Center for Theoretical Biological Physics, Rice University, Houston, Texas 77005, USA*

I. TOPOLOGY OF OUR MODEL

Our topological model for biological oscillations resembles models typically studied in condensed matter physics, owing to its lattice structure. In turn, theoretical results and phenomena from the studies of topology in electronic systems often have direct analogs in our stochastic system. As mentioned in the main text, when $\gamma_{ex} \gg \gamma_{in}$ the system is in the topological regime [1]. Systems with nontrivial topology supports edge states [2, 3]. In our model, the edge state corresponds to the steady-state distribution that is localized on the boundary of the state space. The time evolution of the edge states gives rise to dissipationless currents that is topologically protected and robust to obstacles and defects [4–6]. The analog in our model is the global probability current along the edge of the configuration space. As shown in Fig. S1, in the topological regime the probability current of our stochastic model inherits this property and continues to propagate along the new edge when certain states in the lattice are missing (also see Tang *et al.* [1]). This robustness could explain how biological systems maintain stable dynamics in the face of changing external conditions.

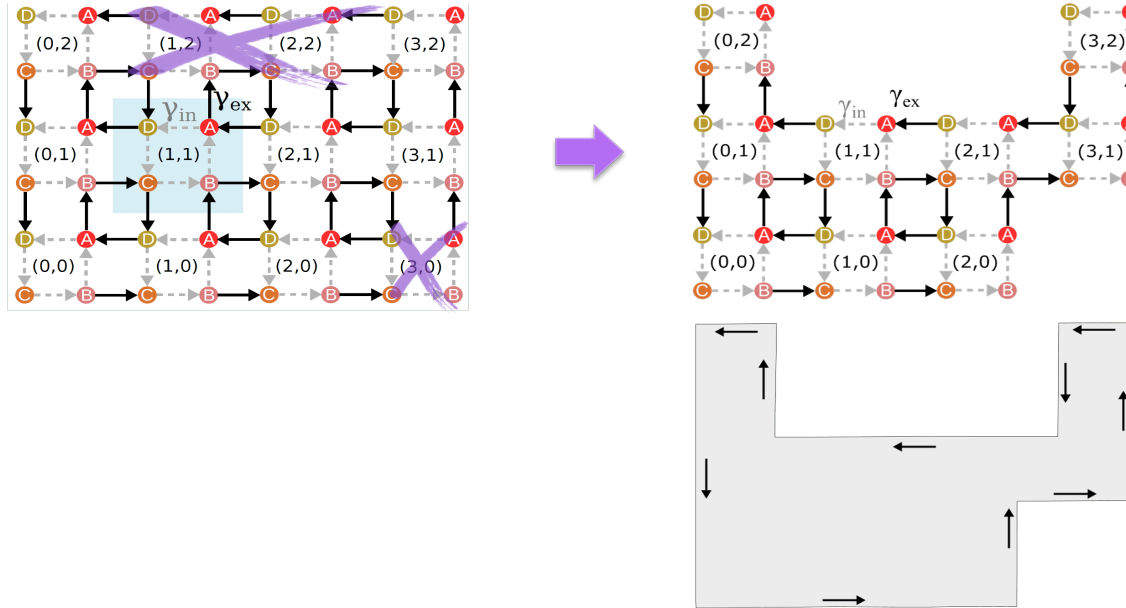


FIG. S1. Topological protection ensures robustness of the edge state to obstacles or missing components. In the presence of missing components or obstacles (purple crosses), the edge state (when $\gamma_{ex} \gg \gamma_{in}$) will simply go around them to maintain the largest available phase space. This robustness of the edge state can shed light on how biological systems can flexibly pivot in the presence of changing conditions or external stimuli.

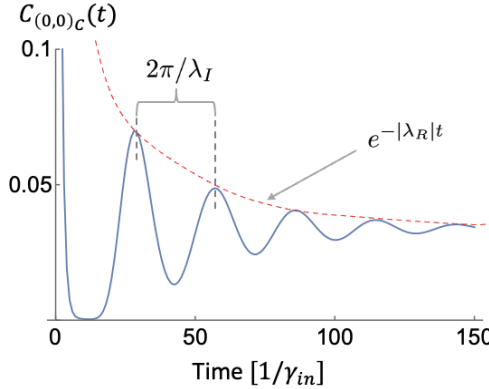


FIG. S2. **Correlation function $C_{(0,0)C}(t)$ for the topological model goes through damped oscillations.** The oscillation has a decay time $|\lambda_R^{-1}|$ and period $2\pi/\lambda_I$. Coherence is defined as the ratio between these two timescales, characterizing the number of coherent oscillations that can be maintained before approaching steady-state. Eventually, $C_{(0,0)C}(t)$ approaches the steady-state probability p_i^s . Time is plotted in units of $1/\gamma_{in}$. The parameters used are $\mu = 7, \rho = 5$.

II. COHERENCE

In this section we motivate the definition of coherence in Eq. (2) in the main text and discuss why it can serve as a measure for the robustness of oscillations. We also discuss how coherence changes with the parameters μ and ρ .

For a master equation with non-degenerate eigenvalues

$$\frac{d\mathbf{p}}{dt} = \mathcal{W}\mathbf{p}, \quad (\text{S1})$$

the general solution is given by

$$p_i(t) = \sum_{\nu} c_{\nu} u_i^{\nu} e^{-\lambda_{\nu} t}, \quad (\text{S2})$$

where λ_{ν} are the eigenvalues, $(u_1^{\nu}, u_2^{\nu}, \dots, u_n^{\nu})^T$ are eigenvectors corresponding to λ_{ν} , and c_{ν} are constant coefficients that depend on initial conditions [7]. The eigenvalues λ_{ν} of the transition matrix \mathcal{W} characterizes the timescales of the probability evolution for the corresponding eigenmodes. If the network represented by \mathcal{W} is irreducible and ergodic, then there exists a unique steady-state distribution \mathbf{p}^s such that $\mathcal{W}\mathbf{p}^s = 0$, i.e., \mathbf{p}^s is an eigenvector of \mathcal{W} with a zero eigenvalue [7]. The dynamics of $\mathbf{p}(t)$, as we will see soon, is in general dominated by the first non-zero eigenvalue of \mathcal{W} , $\lambda_1 \equiv \lambda_R + i\lambda_I$, where λ_R and λ_I are the real and imaginary part of λ_1 , respectively [8].

The dynamics of the system can be studied through correlation functions $C_i(t)$. Following [8], we define $C_i(t)$ to be the probability to find the system at state i at time t given that the system starts at state i at time $t = 0$. More quantitatively, $C_i(t) = p_i(t)$ given the initial condition $p_i(0) = 1$ and $p_j(0) = 0$ for all $j \neq i$. Starting from a state on the edge, say, the lower left corner $(0,0)_C$, the correlation function $C_{(0,0)C}(t)$ goes through damped oscillations (see Fig. S2). After some transient behavior in the first oscillation cycle, the dynamics is dominated by λ_1 , where the oscillation period is given by $T = 2\pi/\lambda_I$ and the exponentially decaying envelope has a decay time $|\lambda_R^{-1}|$ [8]. Therefore, we follow [8] and define coherence as

$$\mathcal{R} \equiv \left| \frac{\lambda_I}{\lambda_R} \right|, \quad (\text{S3})$$

which, when divided by 2π , is the number of coherent oscillations that can be sustained before the system settles into the steady-state. The larger \mathcal{R} is, the more oscillations the system can maintain before stochastic fluctuations destroy its coherence.

In Fig. S3, we show a phase diagram for \mathcal{R} that include negative values of ρ . \mathcal{R} turns out to be monotonic in both μ and ρ . \mathcal{R} increases monotonically in μ because a higher μ implies that the faster reactions would dominate more over their reverse reactions, which is more likely to give rise to trajectories with a particular chirality in our model. These trajectories correspond to the robust oscillations observed, and are less likely to backtrack or perform undirected diffusive motion when the external driving μ is large. For ρ , we can see that \mathcal{R} is always close to zero for $\rho < 0$. Large values of coherence is obtained only with positive ρ , even if the thermodynamic force μ is large.

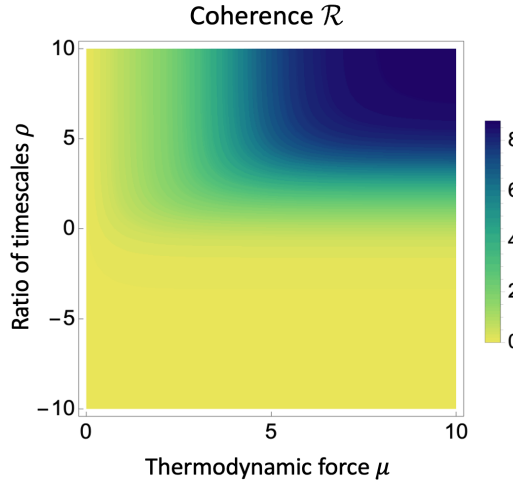


FIG. S3. **Phase diagram for coherence.** The range of ρ is extended from that of Fig. 2a to include negative values. \mathcal{R} is monotonic in both μ and ρ , and remain close to 0 in the trivial regime $\rho < 0$.

This is expected because $\rho \sim 0$ is the transition that separates the topological regime from the trivial regime. In the trivial regime, the system does not support an edge state, and the dynamics resembles random diffusion in the bulk rather than a directed motion along the boundary. Since there are no global oscillations in this regime, the coherence remains low. When ρ is positive and increasing, the system moves deeper into the topological regime, where the edge localization effects are more pronounced, leading to more robust oscillations.

III. SINGLE-MOLECULE MODELS FOR KAIC

In this section, we include more details on the MWC model and the bilayer lattice model mentioned in the main text. Both models can be represented as directed networks and their dynamics described by corresponding master equations.

The MWC paradigm [9] was first applied to the KaiABC system by van Zon *et al.* [10], which assumed all-or-none conformational change for the entire KaiC hexamer. By assumption, the KaiC hexamer can only be in two conformational states, the active states C_i and the inactive states \tilde{C}_i , where the subscript $0 \leq i \leq 6$ represents the phosphorylation level of KaiC. There are 14 states in the state space in total. The network structure is shown in Fig. S4a.

In this paper we follow one of the simplest versions of MWC-type models described in [8] and use the same parametrization of the transition rates. When KaiC is in the active state, it is more likely to be phosphorylated. On the other hand, when KaiC is in the inactive state, it is more likely to be dephosphorylated. These dominant reactions are represented by the red vertical arrows in Fig. S4a with transition rates $\gamma e^{\eta/2}$. The reverse transitions (the smaller black vertical arrows) have rates $\gamma e^{E/6}$. γ , η , and E are model parameters that can be varied. For the horizontal transitions in Fig. S4a, the rates from C_i to \tilde{C}_i are $ke^{\chi E(i-3)/3}$ and the rates from \tilde{C}_i to C_i are $ke^{\tilde{\chi} E(3-i)/3}$, where

$$\chi = \begin{cases} 0, & i = 0, 1, 2, 3 \\ 1, & i = 4, 5, 6 \end{cases} \quad (S4)$$

and

$$\tilde{\chi} = \begin{cases} 1, & i = 0, 1, 2, 3 \\ 0, & i = 4, 5, 6 \end{cases} \quad (S5)$$

The ratio of γ and k sets the relative timescales between the phosphorylation/dephosphorylation reactions and conformational changes. Following [8], we take $k = 1$.

In Fig. S4b we show the network structure for the bilayer lattice model, adapted from Li *et al.* [11]. The state space consists of two layers of 7×7 lattices that are connected to each other. The left panel in Fig. S4b shows the

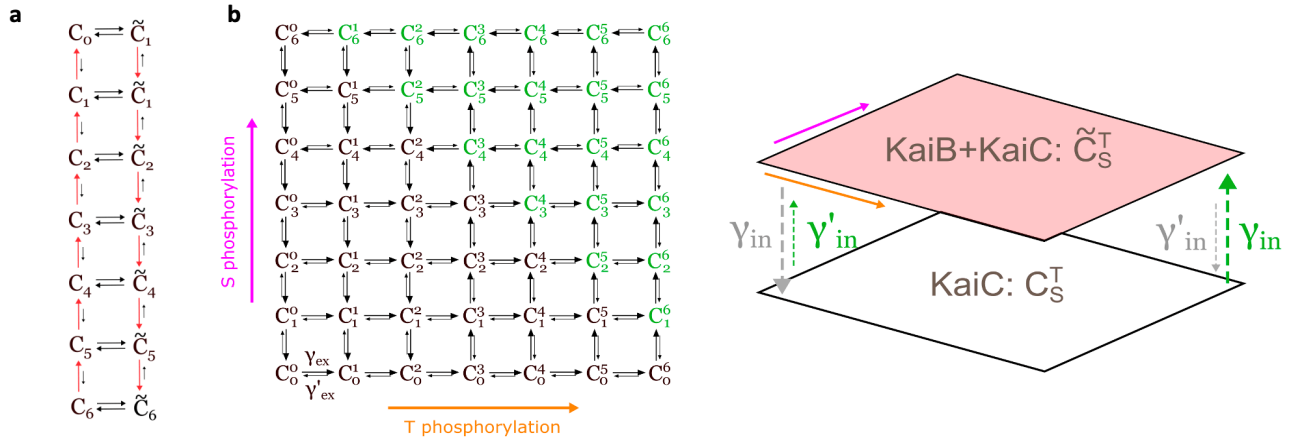


FIG. S4. Single-molecule models for KaiC. **a**, The MWC model. The KaiC hexamer can be in one of two conformation states, the active state C_i or the inactive state \tilde{C}_i . KaiC tends to phosphorylate in the active state and dephosphorylate in the inactive state. **b**, Left panel: the bottom layer of the bilayer lattice model. x and y coordinates represent T and S phosphorylation, respectively, just as for the topological model. Right panel: a zoomed-out view of the bilayer lattice model. Individual states in each layer is not shown. Transitions between layers γ_{in} and γ'_{in} represent KaiB binding and unbinding, during which the phosphorylation levels remain the same.

bottom layer in the right panel. Again, the x and y coordinates (labeled by superscripts and subscripts C_y^x in Fig. S4b) represent T and S phosphorylation levels, respectively. The top layer has an identical structure to the bottom layer, with states labeled by \tilde{C}_y^x . C_y^x in the bottom layer correspond to unbound KaiC while \tilde{C}_y^x in the top layer represent KaiB-bound KaiC. The system can make transitions $C_y^x \rightleftharpoons \tilde{C}_y^x$ between layers while keeping x and y coordinates fixed, which corresponds to KaiB binding and unbinding. To aid comparison, we simplify the model by parametrizing the transition rates with μ and ρ , the same parameters for our topological model. Within both layers, the orientations for faster reactions for each edge are chosen such that they form an overall counterclockwise cycle, to capture the order of the phosphorylation cycle. These transitions are assumed to have uniform rates γ_{ex} while the slower reverse transitions have rates γ'_{ex} . On the other hand, the between-layer KaiB-binding transitions have rates γ_{in} and γ'_{in} . In the upper right half of the lattice where the states are labeled green (left panel of Fig. S4b), the dominant reaction γ_{in} is the upward KaiB binding transition. This is consistent with the fact that S phosphorylation promotes KaiB binding [12]. In the rest of the lattice where the states are labeled black, the dominant reaction is the downward KaiB unbinding transition. This parametrization scheme gives rise to cycles where a KaiC molecule phosphorylates in the bottom layer, binds to KaiB, gets dephosphorylated in the top layer, and unbinds with KaiB to restart the cycle.

IV. COST AND PRECISION FOR DIFFERENT KAIC MODELS

In this section we discuss how the free energy cost (quantified by ΔS) and the precision (quantified by \mathcal{R}) of various KaiC models change with the external driving μ . For the MWC model, the entropy production rate σ of the network can be obtained by a cycle decomposition method [7]:

$$\sigma = \eta\gamma \sum_{i=0}^5 (e^{\eta/2} p_{C_i}^s - e^{E/6} p_{C_{i+1}}^s), \quad (\text{S6})$$

where $p_{C_i}^s$ is the steady-state probability at the state C_i [8]. This expression is used to calculate the entropy production per period $\Delta S = \sigma\mathcal{T}$ for the MWC model. As shown in the left column of Fig. S5, ΔS monotonically increases with \mathcal{R} , as expected. Coherence, however, is not monotonic in μ . When μ is sufficiently large, the MWC model ends up maintaining less coherent oscillations with increased driving and energetic cost. On the other hand, for the topological model, coherence increases monotonically in μ while ΔS is non-monotonic, supporting a regime with increasing coherence and simultaneously decreasing cost (right column of Fig. S5). This unusual regime has its origin from the topological protection of the probability currents on the edge, which effectively reduces the state space into a one-dimensional cycle along the edge. This edge localization leads to a lower free energy cost but more coherent oscillations.

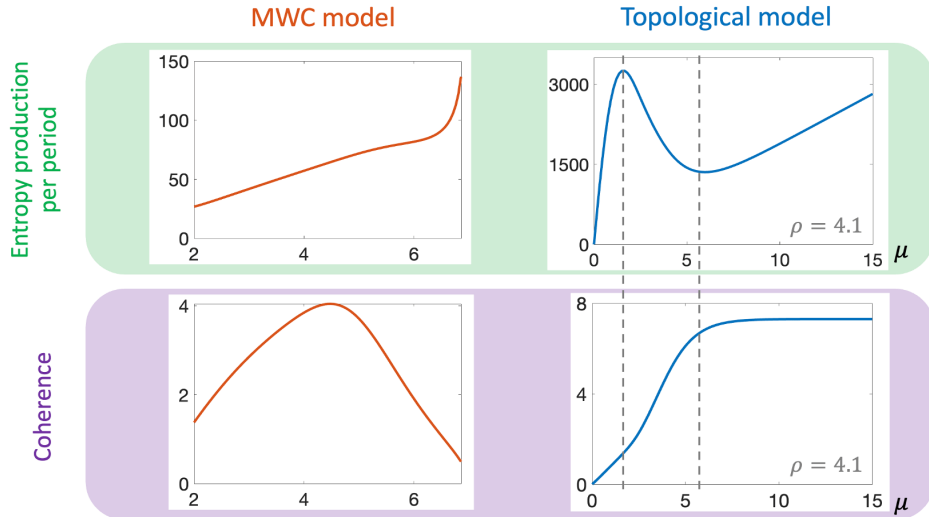


FIG. S5. **Entropy production per period and coherence for the MWC and the topological model.** The MWC model requires more entropy production to maintain a higher coherence, and its coherence decreases as still more entropy is produced under a stronger driving μ . On the other hand, the topological model supports a regime with increasing coherence but decreasing entropy production. For the MWC model, the parameters used are $\gamma = e^5$, $E = 10$. Entropy production per period for the topological model is given in units of $k_B\gamma_{tot}$

V. SPECTRAL GAP AS A PREDICTOR OF COHERENCE

In this section we study the effects of μ and ρ on the spectral gaps of the transition matrix \mathcal{W} with both periodic boundary conditions (PBC) and open boundary conditions (OBC), by tracking how the eigenvalues change with the two parameters. We also discuss why the spectral gap can serve as a predictor of coherence.

Spectral gaps can be defined for both PBC and OBC. Taking PBC, we can write the transition matrix in reciprocal space as

$$\mathcal{W}_k = \begin{pmatrix} -\gamma_{tot} & \gamma_{in} + \gamma'_{ex}e^{-ik_y} & 0 & \gamma'_{in} + \gamma_{ex}e^{-ik_x} \\ \gamma'_{in} + \gamma_{ex}e^{ik_y} & -\gamma_{tot} & \gamma_{in} + \gamma'_{ex}e^{-ik_x} & 0 \\ 0 & \gamma'_{in} + \gamma_{ex}e^{ik_x} & -\gamma_{tot} & \gamma_{in} + \gamma'_{ex}e^{ik_y} \\ \gamma_{in} + \gamma'_{ex}e^{ik_x} & 0 & \gamma'_{in} + \gamma_{ex}e^{-ik_y} & -\gamma_{tot} \end{pmatrix}. \quad (S7)$$

We obtain the spectral gaps for PBC from the continuous spectrum defined by \mathcal{W}_k , as illustrated in Figs. 3a and 3b in the main text. Similarly, we can obtain spectral gaps for OBC by plotting the spectrum of \mathcal{W} in the complex plane, as in Fig. S6a. Apart from the edge states that form two circle-like shapes (red dots), there are four clusters of eigenvalues lying on the real or imaginary axis, which we take to be the four bands in the OBC case. As shown in the figure, for OBC we define the real spectral gap Δ_R as the shortest distance from the leftmost band to the imaginary axis and the imaginary spectral gap Δ_I as the shortest distance from the topmost band to the real axis.

In Fig. S6b we compare the imaginary spectral gap for PBC and OBC for the same parameters μ and ρ . The two gaps are almost identical at large ρ when the gap is large. When ρ is closer to 0, overlaps between the bands begin to develop for both PBC and OBC, which renders the spectral gap ill-defined. In the regime of relatively large ρ , spectral gaps for the OBC and PBC can be used interchangeably. The same conclusion can be drawn by looking at the two gaps with changing μ and fixed ρ . Therefore, to understand the relationship between coherence and the spectral gap, we can look at the OBC spectrum instead.

Studying how λ_1 and the entire OBC spectrum change with μ and ρ gives a better picture of why coherence and the imaginary spectral gap track each other. Varying μ and ρ leads to global changes in the spectrum of \mathcal{W} in the complex plane, such as narrowing of the bandwidth or movement of all eigenvalues in a band in the same direction. Meanwhile λ_1 , the particular eigenvalue that determines coherence (see Fig. S6a), moves along with the bands in roughly the same way. When ρ is fixed, increasing μ has the effect of increasing the range or dispersion of the spectrum in the imaginary part. When $\mu = 0$, all reactions have symmetric rates with respect to their reverse reactions, and the system is in detailed balance. In this case, the spectrum is entirely real because \mathcal{W} is symmetric. Increasing μ therefore introduces nonzero imaginary parts to the eigenvalues, leading to oscillatory modes with faster timescales as the driving increases. For the top band, for instance, the imaginary parts of all eigenvalues in the band move

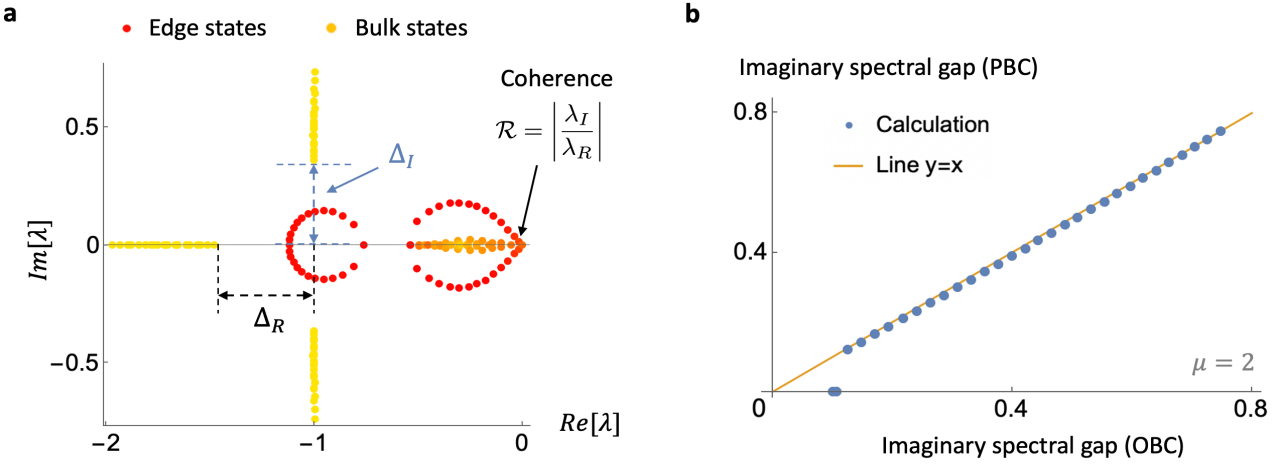


FIG. S6. **Spectral properties of \mathcal{W} in open boundary conditions.** **a**, Spectrum of \mathcal{W} in OBC. The real spectral gap is defined as the shortest distance between the left band to the imaginary axis, and the imaginary spectral gap is defined as the shortest distance between the top band to the real axis. The color for each dot measures the extent to which the corresponding eigenvector is localized on the boundary of the system. The localization is characterized by calculating the sum of the magnitude squared of the elements in the steady-state eigenvector that lie on the edge. A redder color means that the eigenvector is more localized on the edge. The parameters used are $\mu = 2$, $\rho = 1$. **b**, The spectral gaps defined in PBC and OBC are nearly identical when both gaps are large and the bands are well separated. ρ is varied in the plot while μ is fixed at $\mu = 2$. Calculated values for the two gaps in the topological model (blue dots) almost all lie on the orange line on which the two gaps are equal. Eigenvalues and spectral gaps are given in units of γ_{tot} .

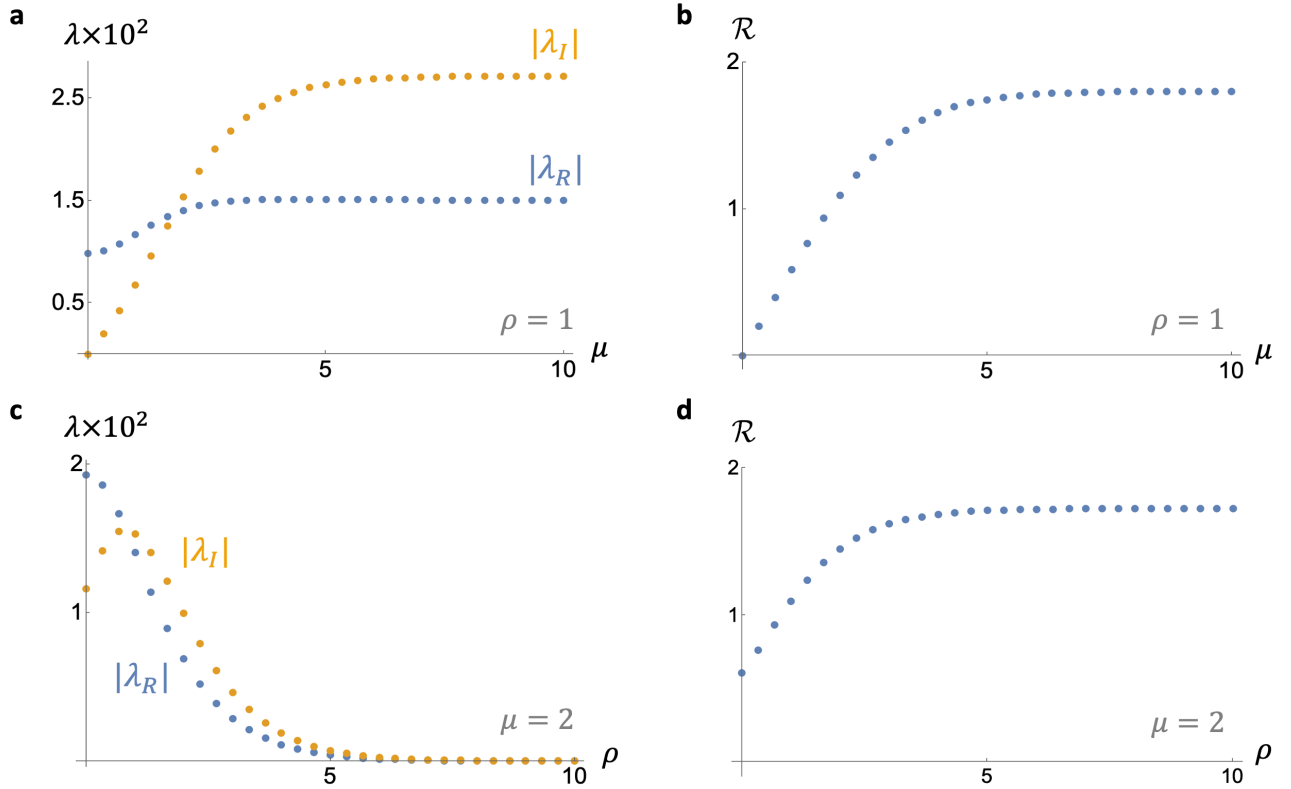


FIG. S7. **Effects of μ and ρ on the first non-zero eigenvalue λ_1 and coherence.** **a**, The absolute value of the real and imaginary parts of $\lambda_1 = 1$ as a function of μ . $|\lambda_I|$ increases with μ and approaches a maximum while $|\lambda_R|$ does not change significantly. **b**, Coherence as a function of μ . \mathcal{R} is almost proportional to $|\lambda_I|$ given a nearly constant λ_R . **c**, The absolute value of the real and imaginary parts of λ_1 as a function of ρ . $|\lambda_R|$ decreases monotonically while $|\lambda_I|$ is non-monotonic in ρ . In the regime where $|\lambda_I|$ decreases, it decreases slower than $|\lambda_R|$. **d**, Coherence as a function of ρ , showing a monotonic increase just as in the μ direction. Eigenvalues are given in units of γ_{tot} .

upwards in the complex plane by roughly the same distance, keeping the bandwidth constant but increasing the distance between the bottom point in the band to the real axis (which is the definition of Δ_I). Meanwhile, the real parts of the eigenvalues in the four bands remain virtually unchanged with μ . As shown in Fig. S7a, λ_1 moves in a similar way with the global spectrum. Increasing μ leads to an increase in $|\lambda_I|$ but very little change in $|\lambda_R|$. Since \mathcal{R} is proportional to $|\lambda_I|$ while $|\lambda_R|$ is roughly constant, coherence follows the same functional relationship as $|\lambda_I|$ when μ increases (Fig. S7b). Therefore, since Δ_I closely tracks $|\lambda_I|$ (see Fig. 3c in the main text), it also closely tracks \mathcal{R} monotonically.

On the other hand, ρ serves as an overall compression factor, decreasing the bandwidth for all four bands. The points furthest away from the real axis for the imaginary bands also increase slightly with ρ . The absolute values of these points equal the sum of the bandwidth for the imaginary band and the imaginary spectral gap. Therefore, a decrease in the bandwidth and an increase in the sum of the bandwidth and the spectral gap imply a monotonic increase in the spectral gap with increasing ρ . λ_1 in this case, however, does not always follow the general movement of the global spectrum. As shown in Fig. S7c, $|\lambda_R|$ still decreases monotonically as expected, as the rightmost band is compressed toward the origin. $|\lambda_I|$, on the other hand, develops non-monotonic behavior. Nevertheless, when $|\lambda_I|$ begins to decrease, it vanishes more slowly than $|\lambda_R|$ and gives rise to a monotonically increasing \mathcal{R} that tracks Δ_I in ρ (Fig. S7d).

[1] E. Tang, J. Agudo-Canalejo, and R. Golestanian, Topology protects chiral edge currents in stochastic systems, *Physical Review X* **11**, 031015 (2021).

[2] Y. Hatsugai, Chern number and edge states in the integer quantum hall effect, *Physical review letters* **71**, 3697 (1993).

[3] M. Z. Hasan and C. L. Kane, Colloquium: topological insulators, *Reviews of modern physics* **82**, 3045 (2010).

[4] B. I. Halperin, Quantized hall conductance, current-carrying edge states, and the existence of extended states in a two-dimensional disordered potential, *Physical Review B* **25**, 2185 (1982).

[5] C. L. Kane and E. J. Mele, Quantum spin hall effect in graphene, *Physical review letters* **95**, 226801 (2005).

[6] J. E. Moore, The birth of topological insulators, *Nature* **464**, 194 (2010).

[7] J. Schnakenberg, Network theory of microscopic and macroscopic behavior of master equation systems, *Reviews of Modern Physics* **48**, 571 (1976).

[8] A. C. Barato and U. Seifert, Coherence of biochemical oscillations is bounded by driving force and network topology, *Physical Review E* **95**, 062409 (2017).

[9] J. Monod, J. Wyman, and J.-P. Changeux, On the nature of allosteric transitions: a plausible model, *Journal of molecular biology* **12**, 88 (1965).

[10] J. S. van Zon, D. K. Lubensky, P. R. Altena, and P. R. ten Wolde, An allosteric model of circadian KaiC phosphorylation, *Proceedings of the National Academy of Sciences* **104**, 7420 (2007).

[11] C. Li, X. Chen, P. Wang, and W. Wang, Circadian KaiC phosphorylation: a multi-layer network, *PLoS computational biology* **5**, e1000568 (2009).

[12] G. K. Chow, A. G. Chavan, J. Heisler, Y.-G. Chang, N. Zhang, A. LiWang, and R. D. Britt, A night-time edge site intermediate in the cyanobacterial circadian clock identified by EPR spectroscopy, *Journal of the American Chemical Society* **144**, 184 (2022).